The optoelectronic microrobot: A versatile toolbox for micromanipulation

Shuailong Zhang[a,b,c], Erica Y. Scott[a,b,c], Jastaranpreet Singh[a,c], Yujie Chen[d], Yanfeng Zhang[d], Mohamed Elsayed[a,c], M. Dean Chamberlain[a,b,c], Nika Shakiba[a,c], Kelsey Adams[a,e], Siyuan Yu[d,f], Cindi M. Morshead[a,c,e,g], Peter W. Zandstra[a,c,h,i,j], and Aaron R. Wheeler[a,b,c,1]

[a]Donnelly Centre for Cellular and Biomolecular Research, University of Toronto, Toronto, ON M5S 3E1, Canada; [b]Department of Chemistry, University of Toronto, Toronto, ON M5S 3H6, Canada; [c]Institute for Biomaterials and Biomedical Engineering, University of Toronto, Toronto, ON M5S 3G9, Canada; [d]State Key Laboratory of Optoelectronic Materials and Technologies, School of Electronics and Information Technology, Sun Yat-sen University, 510275 Guangzhou, China; [e]Institute of Medical Sciences, University of Toronto, Toronto, ON M5S 1A8, Canada; [f]Photonics Group, Merchant Venturers School of Engineering, University of Bristol, BS8 1UB Bristol, United Kingdom; [g]Department of Surgery, University of Toronto, Toronto, ON M5T 1P5, Canada; [h]School of Biomedical Engineering, University of British Columbia, Vancouver, BC V6T 1Z3, Canada; [i]The Biomedical Research Centre, University of British Columbia, Vancouver, BC V6T 1Z3, Canada; and [j]Michael Smith Laboratories, University of British Columbia, Vancouver, BC V6T 1Z4, Canada

Edited by John A. Rogers, Northwestern University, Evanston, IL, and approved June 14, 2019 (received for review February 27, 2019)

Microrobotics extends the reach of human-controlled machines to submillimeter dimensions. We introduce a microrobot that relies on optoelectronic tweezers (OET) that is straightforward to manufacture, can take nearly any desirable shape or form, and can be programmed to carry out sophisticated, multiaxis operations. One particularly useful program is a serial combination of "load," "transport," and "deliver," which can be applied to manipulate a wide range of micrometer-dimension payloads. Importantly, microrobots programmed in this manner are much gentler on fragile mammalian cells than conventional OET techniques. The microrobotic system described here was demonstrated to be useful for single-cell isolation, clonal expansion, RNA sequencing, manipulation within enclosed systems, controlling cell–cell interactions, and isolating precious microtissues from heterogeneous mixtures. We propose that the optoelectronic microrobotic system, which can be implemented using a microscope and consumer-grade optical projector, will be useful for a wide range of applications in the life sciences and beyond.

microrobotics | optoelectronic tweezers | dielectrophoresis | single-cell manipulation | single-cell RNA sequencing

Robotics is commonly defined as the design, construction, and use of machines that can substitute for humans and replicate human actions. An important concept in robotics is multifunctionality (1–3)—that is, many robots are able to carry out complex, diverse tasks depending on the (potentially changing) needs of the operator. "Microrobotics" extends the reach of robotic operations to submillimeter (sub-mm) dimensions, and a key goal in microrobotics is the capacity to control primary sub-mm particles or "robots," such that the robots can themselves control the behavior of secondary sub-mm particles or "payloads." (2–6) Microscale (and nanoscale) robotic systems can be subclassified into at least 2 dimensions: force and operator-control/autonomy. For the former, microrobots can be described in terms of the forces that are used to manipulate them—for example, photonic (4–6), magnetic (7–9), and acoustic (10–12) forces. For the latter, microrobots can be described as "passive" or "active" in terms of human control over their operations—for example, the operator has limited control over the behavior of passive (or "swimmer"-type) microrobots (3, 10) (but they are highly autonomous), while the operator has great control over active microrobots (2, 4–9, 11, 12) (but they have less autonomy). Each type of microrobot has advantages and disadvantages that make it more or less suitable for different applications. Here, we introduce an active, photonically controlled microrobot.

Photonic microrobots have traditionally been controlled by optical tweezers (OT) (13), and these systems have been used to carry out complex procedures, including tissue growth (4), translation (5, 6), pumping (14, 15), and surface scanning (16, 17). While these systems are impressive, there are some limitations. OT is only capable of reliably actuating objects with sizes less than 30 μm (a result of the diminutive forces that can be exerted), which sets firm limits on potential applications (particularly for those that involve large objects or payloads). Second, microrobots that are manipulated by OT typically must be fabricated using expensive, time-consuming, and specialized fabrication tools (5, 6, 15–17). Third, while it is possible to manipulate multiple microrobots in parallel with OT (6, 13, 16, 17), this functionality requires specialized beam-shaping optics, expertise, and control software. These challenges are substantial, and are at least part of the reason that OT-controlled microrobots are currently relegated to niche applications.

Here, we introduce a microrobot that is controlled by optoelectronic tweezers (OET) (18–20). Because OET relies on light to control dielectrophoresis (DEP) rather than relying on forces generated by direct photon momentum, OET systems typically exert a stronger manipulation force for a given intensity of light compared with OT (20, 21). In addition, the light patterns used in OET can be generated with consumer-grade optical projectors, making it widely accessible and well suited for parallel manipulation (18, 20, 22). OET has been used previously for

Significance

There is great interest in robotic systems that can substitute for humans and replicate human actions. "Microrobotics" describes robotic systems that have submillimeter (sub-mm) dimensions, which is becoming increasingly important for the manipulation and analysis of individual cells and groups of cells. Here we introduce the optoelectronic microrobot, a system in which projected patterns of light are applied to control electric fields. Specially designed microrobots respond to the fields, and can be programmed to move and "scoop up" mammalian cells or other sub-mm particles such that they can be isolated and evaluated independently. The technique is straightforward to implement, and we propose will find wide use for the ever-expanding list of applications that require micromanipulation of cells.

Author contributions: S.Z., C.M.M., P.W.Z., and A.R.W. designed research; S.Z., E.Y.S., J.S., Y.C., Y.Z., M.E., M.D.C., N.S., K.A., and S.Y. performed research; E.Y.S. contributed new reagents/analytic tools; S.Z. and E.Y.S. analyzed data; and S.Z. and A.R.W. wrote the paper.

The authors declare no conflict of interest.

This article is a PNAS Direct Submission.

[1]To whom correspondence may be addressed. Email: aaron.wheeler@utoronto.ca.

This article contains supporting information online at www.pnas.org/lookup/suppl/doi:10.1073/pnas.1903406116/-/DCSupplemental.

Published online July 9, 2019.

a range of applications (18–27); here we describe its extension to microrobotics, and propose that this combination may prove useful for a variety of applications.

Results and Discussion

All OET work reported previously has relied on direct manipulation of objects of interest (18–29). Here, we report the use of OET to manipulate microrobots, which are in turn used to manipulate secondary objects in multiaxis, multistep operations. Fig. 1*A* depicts a cross-sectional schematic of one of the microrobots; because arrays of microrobots can be generated in parallel, this procedure is extremely efficient, allowing for the generation of tens of thousands of microrobots in about an hour of work. This is inherently faster than the serial techniques that are used to form the smaller microrobots that are actuated by OT (5, 6, 15–17).

Microrobots with 3 different geometries were used in this work. Fig. 1 *B* and *C* show representative scanning electron microscope (SEM) images of "cogwheel"-shaped microrobots, bearing a semienclosed central chamber with an opening on one side. This motif has been used in the microfluidic community for many years to trap single cells and particles (30–33); the critical advance here is that the structure is movable (rather than stationary). Fig. 1 *D*–*G* shows representative SEM images of 2 other microrobot geometries used here—a "box" design and a "spaceship" design, also bearing semienclosed chambers. Note that each of the microrobots is more than 200 μm across, much larger than objects that that can be manipulated by OT-based techniques. The 3 designs were selected to serve as examples; the range of geometries is virtually unlimited.

After fabrication, the microrobots were transferred to a microscopy platform in which light patterns originating from a consumer-grade projector are focused onto an OET device bearing a photoconductor [in this case, a layer of hydrogenated amorphous silicon, a-Si:H (28, 29)]. As shown in Fig. 1 *H*–*J*, the light patterns were designed to form a negative relief of the perimeter of each microrobot; for the parameters and materials used here, this results in a "negative" DEP force that focuses the microrobots into the "dark" centers of the projected patterns. As illustrated in Movies S1 and S2, microrobots were made to move across the device (at a given linear velocity in a horizontal axis) by translating a device relative to a light pattern that was held stationary, and/or to rotate (at a given angular velocity around a central axis) by spinning the projected image relative to a device that was held stationary. For either operation (translation or rotation), the negative DEP forces were sufficient to cause the robots to move at low velocities. As the velocities were increased, the microrobots began to resist motion until they reached a "maximum" velocity at which they escaped the trap [a phenomenon described in detail in previous work (29)].

The maximum linear and angular velocities (as a function of bias voltage) are shown in Fig. 1 *K*–*M*. For example, a maximum linear velocity of 1.1 mm/s and a maximum angular velocity of 9.7 rad/s was observed for the cogwheel-shaped microrobot driven at a bias of 25 $V_{p\text{-}p}$ at 20 kHz (Fig. 1*K*). In general, all of the microrobots were movable at low velocities, the cogwheel- and box-shaped microrobots were movable at high linear velocities (greater than 1 mm/s), and only the cogwheel-shaped microrobot was movable at high angular velocities (greater than 9 rad/s). Microrobot movement was also evaluated for microrobots with different heights—those that are too short (e.g., 30 μm) or too tall (e.g., 100 μm) are less stable than those with heights that are between the 2 extremes (*SI Appendix*, Fig. S1 *A*–*C*). Finally, movement was evaluated for microrobots formed from different materials (e.g., silver nanoparticle-doped epoxy, *SI Appendix*, Fig. S1*D*). Cogwheel-shaped robots formed from unmodified SU-8 (with 50-μm height) were used for the remainder of the work, but the

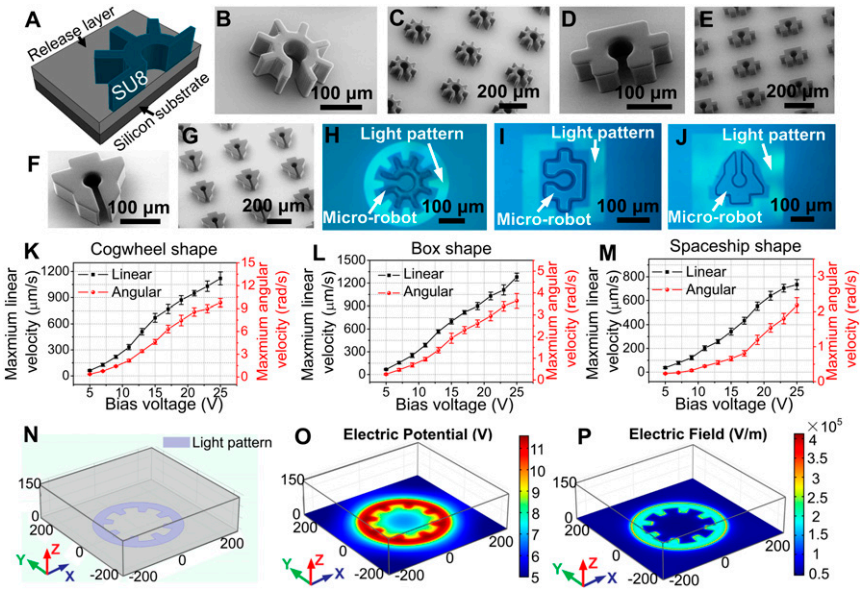

Fig. 1. Optoelectronic microrobots. (*A*) Cross-sectional schematic of a cogwheel-shaped microrobot, formed from SU-8 on a sacrificial release layer. (*B*) SEM image of a cogwheel-shaped microrobot. (*C*) SEM image of an array of cogwheel-shaped microrobots. (*D*–*G*) SEM images of box-shaped and spaceship-shaped microrobots. Bright-field microscope images of (*H*) a cogwheel-shaped microrobot, (*I*) a box-shaped microrobot, and (*J*) a spaceship-shaped microrobot held in place by OET light patterns. Illuminated and nonilluminated regions appear light and dark, respectively. Maximum linear (left axis, black) and angular (right axis, red) velocities as a function of OET bias voltage for translating and rotating (*K*) cogwheel-shaped microrobots, (*L*) box-shaped microrobots, and (*M*) spaceship-shaped microrobots (Movies S1 and S2). Error bars represent ±1 SD from 5 measurements for each condition. (*N*) Three-dimensional simulation of an OET device in which a light pattern (purple) is projected onto an a-Si:H surface. XY plots at Z = 1.1 μm of simulated (*O*) electric potential distribution and (*P*) electric field distribution for a device driven at 20 $V_{p\text{-}p}$ (25 kHz), in which the simulated electric potential and field are indicated in heat maps (blue = low, red = high). The axis dimensions in *N*-*P* are in micrometers.

flexibility in shape, material, and height suggests tunability for a wide range of applications in the future.

As a step toward understanding optoelectronic microrobot behavior, a 3D numerical simulation (28, 29) was developed (Fig. 1 *N*–*P*). As expected, the electric field gradient is very high at the edges of the projected pattern. Because DEP force scales with the square of the electric field gradient (21, 23–28), and because trapped objects with longer perimeters are exposed to more of these regions correlated with high DEP force, we hypothesize that the cogwheel-shaped microrobot experiences greater rotational torque because of its increased perimeter. More study is needed given the nature of this complex mechanical–fluidic system with many variables (including weight-related frictional force and DEP force/viscous drag force for irregular mechanical structures). Regardless, the operating principles are straightforward to use and apply, as described below.

Armed with an OET-driven microrobotic system, attention was turned to developing a series of operations relying on combinations of linear and rotational movements using light patterns that fully or partially enclose the microrobots. A particularly useful series of operations was found to be payload loading, transportation, and delivery. This process is illustrated for a 15-μm-diameter polystyrene bead (the payload) in Movie S3 and Fig. 2 *A*–*F*. In this process, a bead was selected and loaded into the microrobot (Fig. 2 *A*–*C*), transported across the device (Fig. 2*D*), and then delivered to its targeted location (Fig. 2 *E* and *F*), all in a matter of seconds. Fig. 2*G* illustrates the spatial relationships in this 6-step process; as indicated, the destination can be long distances from the point of origin.

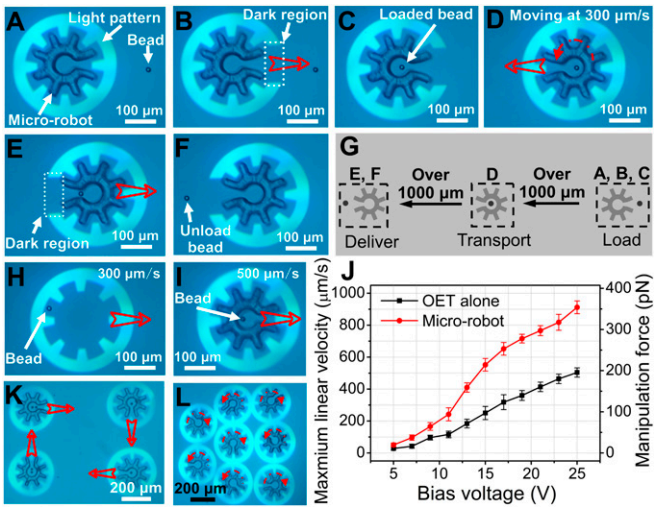

Fig. 2. Microrobot operations. Bright-field microscope images (from Movie S3) of a cogwheel-shaped microrobot and a 15-μm-diameter polystyrene bead, with (*A*) a fully enclosed microrobot being aligned with the bead, (*B*) a partially enclosed microrobot in 'load' mode, (*C*) a partially enclosed microrobot with bead immediately after loading, (*D*) a fully enclosed microrobot and bead in "translate" mode, (*E*) a partially enclosed microrobot midway through the process of "delivery," and (*F*) a partially enclosed microrobot after bead delivery. (*G*) Schematic illustrating the spatial relationship between *A*–*C* (load), *D* (transport), and *E* and *F* (delivery). Bright-field microscope images depicting the manipulation of a 15-μm-diameter polystyrene bead (*H*) by OET alone at 300 μm/s and (*I*) with the microrobot at 500 μm/s. (*J*) Maximum linear velocity (left axis) and corresponding DEP manipulation force (right axis) as a function of bias voltage for a bead translated alone (black) or inside a microrobot (red). Error bars represent ±1 SD from 5 measurements for each condition. Bright-field microscopy images (from Movie S4) demonstrating (*K*) the translation of 4 microrobots bearing payloads (one or two 15-μm-diameter polystyrene beads) in different directions, and (*L*) the rotation of 8 microrobots with each robot rotating at a different angular velocity. In images, open red arrows represent translation and dashed red arrows represent rotation.

Microrobots are not required for bead manipulation, as OET can be used to manipulate a bead on its own or within a microrobot (Fig. 2 *H* and *I*, respectively). To compare these techniques, identical light patterns were used to determine the maximum velocities for 15-μm-diameter beads, which are plotted in Fig. 2*J*. The manipulation force corresponding to each maximum velocity was calculated using Stokes' law (23–29), as described in *SI Appendix*. As shown in Fig. 2*J*, beads manipulated by the microrobot are able to withstand larger viscous forces than those manipulated by OET alone. For example, for a 25 $V_{p\text{-}p}$ bias, beads can withstand ∼350 pN in the microrobot, but only 200 pN before they escape from the OET trap. We believe this difference to be a function of the manipulation force, which for OET-alone originates directly from DEP [determined by interactions between the bead and the electric field (18, 21, 24, 28, 29)], while for the microrobot, the manipulation force originates from the interfacial pressure generated by the inner wall of the structure. This suggests a "universal" force, as any payload, regardless of its Clausius–Mossotti factor (21) (which determines the DEP force experienced by a trapped object), should be manipulatable using the microrobotic technique.

Finally, a key feature in microrobotics is parallel operation. Movie S4 shows simultaneous movement of 4 microrobots on paths toward different destinations, as well as simultaneous rotation of 8 microrobots at different velocities and directions (depicted in Fig. 2 *K* and *L*, respectively). Movie S5 shows similar operations for box-shaped and spaceship-shaped microrobots. As indicated above, the optical projector-based system used here is more straightforward to use for parallel manipulation relative to conventional OT, which typically requires a holographic system with complex control software and optical assembly for parallel operations (6, 16, 17).

After establishing basic optoelectronic microrobot capacity, attention was turned to manipulation of mammalian cells. In initial experiments, ARPE-19 human retinal pigment epithelial cells were prelabeled red and MCF-7 breast cancer cells were prelabeled green, and mixtures were loaded into OET devices. As illustrated by Movie S6 and Fig. 3 *A*–*F*, it was found that any desired combination of cells could be loaded, transported, and delivered using the same methods applied to polystyrene beads, described above. Of course, OET can be used to manipulate a single cell on its own or within a microrobot (Fig. 3 *G* and *H*, respectively). In fact, one of the most popular applications for OET has been the direct manipulation of cells (18, 20, 26, 34, 35). So, why would one want to use the optoelectronic microrobot?

We propose 2 key reasons for using the microrobot to manipulate cells instead of OET alone. The first is the capacity to generate large, uniform forces. This is important, as in (typical) OET conditions, DEP forces generated on cells from OET are small and can vary by cell type. This was probed by determining maximum velocities (and their corresponding forces), which are plotted in Fig. 3*I*. For example, when driven at a 10-$V_{p\text{-}p}$ bias, cells manipulated by the microrobot can withstand ∼90 pN of driving force before they escape, approximately 3 times greater than cells manipulated by OET alone. Furthermore, microrobot cell transport appears to be universal (i.e., independent of cell type, as in the red and blue triangles in Fig. 3*I*), while transport varies by cell type for OET alone (black squares and turquoise circles in Fig. 3*I*). The second reason is the potential to reduce cell damage caused by continuous exposure to bright illumination in OET. This effect has been described previously (28, 36–38), and we devised a unique small-cell-number viability assay to evaluate its potential effect here (*SI Appendix*, Fig. S2). As shown in Fig. 3*J*, viability is nearly unchanged after manipulation by microrobot, but it is reduced to 76% for ARPE-19 cells and 70% for MCF-7 cells when manipulated using OET alone. We

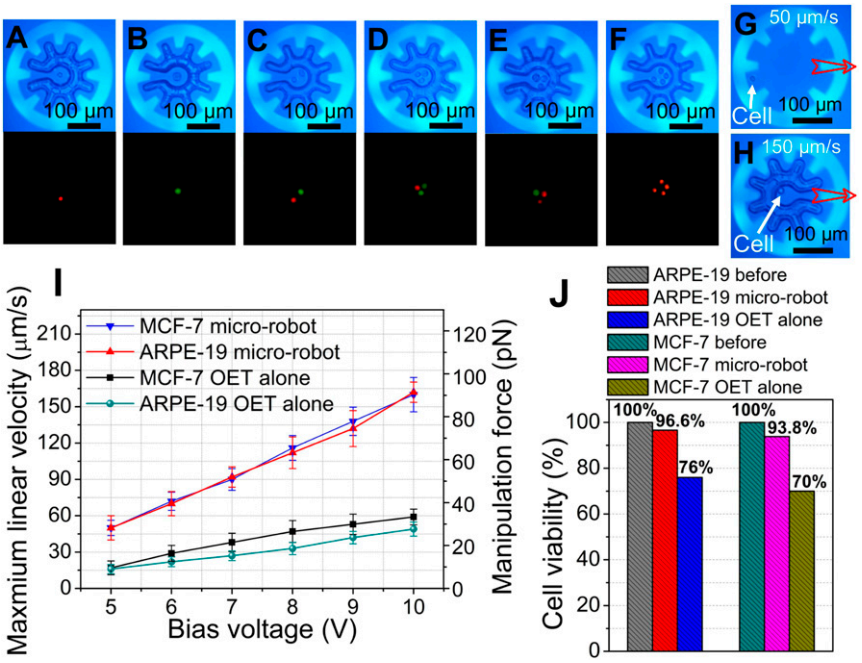

Fig. 3. Microrobot manipulation of mammalian cells. (*A*–*F*) Bright-field (*Top*) and fluorescent (*Bottom*) microscope images (from Movie S6) of different combinations of ARPE-19 cells (prelabeled with red fluorescent dye) and MCF-7 cells (prelabeled with green fluorescent dye) after loading into microrobots. Bright-field microscope images (from Movie S7) depicting the manipulation of a single ARPE-19 cell with (*G*) OET alone at 50 μm/s and (*H*) a microrobot at 150 μm/s. Open red arrows represent translation. (*I*) Maximum linear velocity (left axis) and corresponding DEP manipulation force (right axis) as a function of bias voltage for individual ARPE-19 cells or MCF-7 cells translated by OET alone (turquoise circles or black squares, respectively) or by microrobot (red triangles or blue triangles, respectively). Error bars represent ±1 SD from 5 measurements. (*J*) Cell viability before (gray hatch: ARPE-19; turquoise hatch: MCF-7) and after cells were continuously manipulated at 15 μm/s for 100 s by OET alone (blue hatch: ARPE-19, n = 38/50; yellow hatch: MCF-7, n = 35/50) or a microrobot (red hatch: ARPE-19, n = 28/29; violet hatch: MCF-7, n = 30/32) at an applied bias of 7 $V_{p\text{-}p}$ at 20 kHz. Numbers of cells evaluated in each condition (n) are pooled from 10 replicates of 5 cells each (for OET alone) and 10 replicates of 2 to 5 cells each (for the microrobot).

attribute this effect to exposure to the large electric field at the edge of the light pattern, as well as light-induced heating, which can perforate the cell membrane (36–38). In fact, we find that killing cells by OET is remarkably easy—for example, Movie S8 illustrates nearly instantaneous lysis of MCF-7 cells by OET driven at 18-$V_{p\text{-}p}$ bias voltage; the same movie shows that microrobots driven by the same bias can be used to manipulate cells without harm. The critical difference is positioning—that is, as shown in the simulation in Fig. 1*P*, strong electric fields (up to 4×10^5 V/m) exist only at the edge of the light pattern—cells carried by the microrobot (many micrometers away from the light pattern) experience very low electric field.

After demonstrating optoelectronic microrobotic manipulation of cells, attention was turned to an important application in life-science research—single-cell isolation for clonal expansion. Techniques that are commonly used for this procedure [including serial dilution (39, 40) and flow cytometry/sorting (41)] are arduous and time-consuming, and suffer from inherently low success rates (42). A device bearing semienclosed (and permanent) microwells (35) (Fig. 4*A* and *SI Appendix*, Fig. S3) was used to test this application. Mixtures of B-16 murine tumor cells (red) and U-87 human glioblastoma cells (green) were loaded into the device (Fig. 4*B*), a cell was selected and loaded into a microrobot (Fig. 4*C*), and the robot and payload were transported to a designated microwell (Fig. 4*D*), where the cell was delivered; each such isolation required ∼1 min. Isolated cells were then cultured for several days, and as shown in Fig. 4 *E* and *F*, the cells were observed to begin the process of clonal expansion.

The optoelectronic microrobot was also explored for compatibility with RNA sequencing (RNA-seq). Specifically, microrobots were used to select, transport, and deliver 1 or a few cells from the mixture described above to microwells (*SI Appendix*, Fig. S4*A*), followed by cell lysis, mRNA capture, cDNA synthesis, whole genome amplification, and RNA-seq (*SI Appendix*). For global analysis, t-distributed stochastic neighbor embedding (TSNE) (Fig. 4*G*) and other forms of dimensionality reduction (*SI Appendix*, Fig. S4*B*) demonstrated strong overlap between samples by cell type (as opposed to cell number). These differences are reflected in the distributions of genes identified per sample (*SI Appendix*, Fig. S4*C*) and read-counts per sample (Fig. 4*H*). A subset of the single gene-expression analysis of the 4 samples is summarized in Fig. 4*I*; the corresponding dataset is included in *SI Appendix*, Table S1.

The tasks described above (cell sorting, clonal expansion, and RNA-seq) can be implemented using cutting-edge laser-dissection tools (43) or imaging-based fluidic sorting (44). In its current form, the optoelectronic microrobot cannot compete with these techniques in terms of throughput; on the other hand, these techniques (43, 44) are dedicated tools that can be used only to perform the given operation, while the system described here was designed to fulfill a key goal of robotics, multifunctionality (1–3). This capacity was explored in two additional applications. First, cell-fusion protocols [important in antibody production (45) and cell programming (46)] were developed, using a microfluidic system (*SI Appendix*, Fig. S5). Fig. 5*A* shows the results of 3 cell–cell fusion experiments—1 example each of 2-cell homotypic fusion, 3-cell homotypic fusion, and 2-cell heterotypic fusion, respectively. As shown, in these experiments, the microrobot serves not only as a vehicle for payload selection and transport, but also as the chamber in which the cell fusion is realized. Second, the capacity to select and isolate precious payloads from heterogeneous mixtures (3) was evaluated. As illustrated in Movie S9 (and depicted in Fig. 5 *B* and *C*), the optoelectronic microrobot was found to be a nimble instrument for navigating a maze of debris (i.e., dead cells, aggregates, and cell

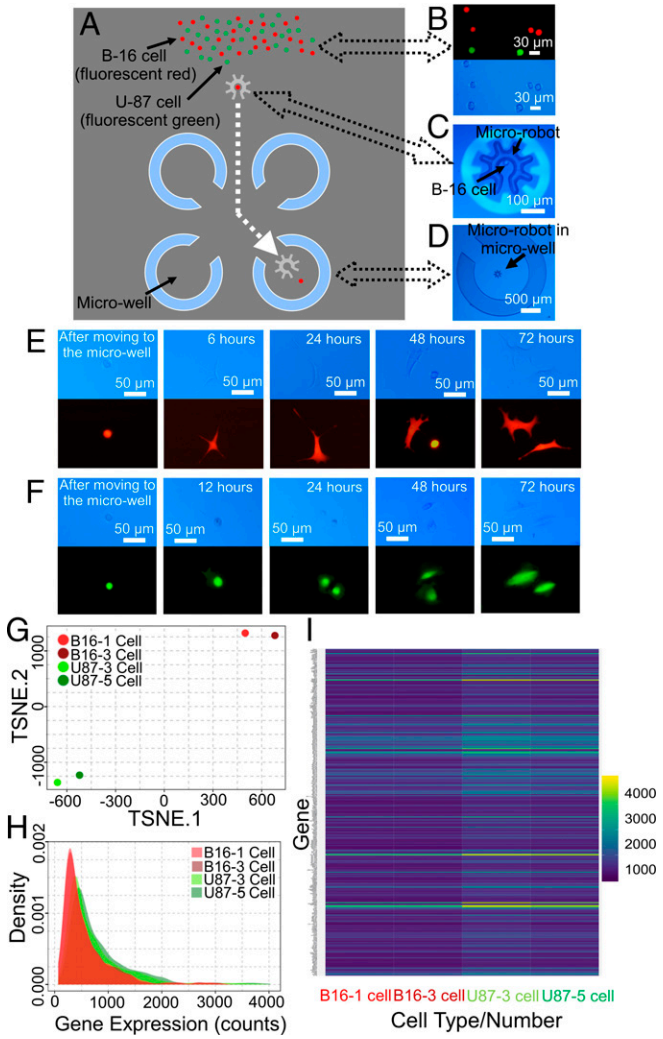

Fig. 4. Microrobots for cell selection, isolation, expansion, and RNA-seq analysis. (*A*) Schematic of device featuring semienclosed microwells (blue). (*B*) Fluorescent (*Top*) and bright-field (*Bottom*) microscope images of a mixture of B-16 cells (red/tdTomato expressing) and U-87 cells (green/eGFP expressing) after loading into the device. (*C*) Bright-field microscope image of a B-16 cell in a microrobot. (*D*) Bright-field microscope image of a microrobot in a microwell. Representative time-dependent bright-field (*Top*) and fluorescent (*Bottom*) microscope images showing (*E*) a B-16 cell and (*F*) a U-87 cell attaching, growing, and dividing after being isolated in a microwell for clonal expansion. (*G*) TSNE dimensionality reduction of the transcriptome for 1 (light-red) or 3 (dark-red) B-16 cells and 3 (light green) or 5 (dark green) U-87 cells, respectively. (*H*) Plots of read density as a function of gene-expression count for the 4 samples. (*I*) Heat map of gene expression (blue: low, yellow: high) for the subset of variable genes with SEM > 30 for the 4 samples (full dataset in *SI Appendix*, Table S1).

fragments) to collect neurospheres (47) (~100-μm-diameter free-floating multicell colonies comprising neural stem cells and their progeny) from primary mouse brain dissections. These applications demonstrate proof of concept; we propose that the optoelectronic microrobot might be used in the future for a diverse set of applications requiring precise, controlled micromanipulation.

Finally, note that in all of the proof-of-concept methods described here, the position of the microrobot was managed via real-time user input to the software controlling the motorized microscope stage and the projector. In ongoing work, we are developing greater levels of automation relying on image recognition algorithms to identify desirable targets for analysis or extraction coupled to preprogrammed operations such as load, transport, and deliver. In the future, the microrobot might be customized to minimize the operator's input [e.g., to enable high-throughput cell selection and analysis (43, 44)]; in other applications, the high level of operator control described here might be preserved for use as a multifunctional toolbox.

Conclusion

We introduce an optoelectronic microrobot for the manipulation of cells and other particles. The system is extremely precise, allowing complex multiaxis operations including load, translate, and delivery of a payload across large distances. Parallel and independent manipulation of multiple microrobots is possible, suggesting the capacity for high-throughput manipulation. The technique was demonstrated to be useful for selection and isolation of single cells for clonal expansion and RNA-seq, selection and targeting of cell–cell fusion partners, and collection of precious microtissue specimens from complex samples. We propose that the unique properties of the optoelectronic microrobot, which can be implemented using a simple microscope and consumer-grade optical projector, will be useful for a wide range of applications in the life sciences and beyond.

Materials and Methods

OET System. Detailed descriptions of the OET instrumentation (a Leica DM 2000 microscope interfaced to a Dell 1650 projector) and devices used here (each featuring a 20 μL enclosed fluidic chamber sandwiched between 2

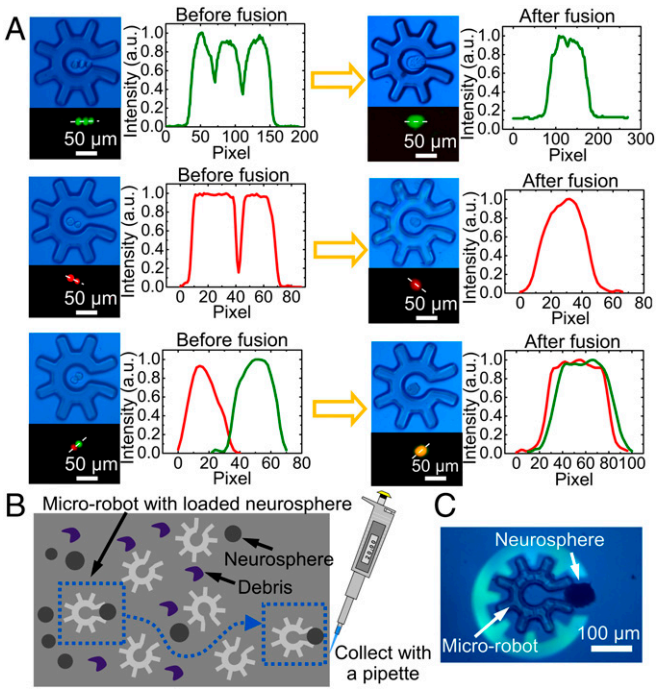

Fig. 5. Microrobots applied to electrofusion and selection from complex samples. (*A*) Left of arrow: bright-field (*Top Left*) and fluorescence (*Bottom Left*) microscopy images, and fluorescence intensity profiles (collected across the white dashed lines in the fluorescence images) (*Right*) of cells collected and isolated in a microrobot. Right of arrow: comparable images/profiles of the same cells after electrofusion. *Top*, *Middle*, and *Bottom* rows feature 3 U87 cells undergoing homotypic fusion, 2 B16 cells undergoing homotypic fusion, and 1 B16/1 U87 cell undergoing heterotypic fusion, respectively. (*B*) Schematic illustration of using a microrobot to navigate a complex environment to collect a targeted neurosphere (left: blue dashed box) to bring it to the destination (right: blue dashed box) for collection. (*C*) Bright-field microscope image (from Movie S9) showing the use of a microrobot to transport a neurosphere.

electrode-bearing plates, with the "bottom" electrode/plate coated with hydrogenated amorphous silicon, a-Si:H) can be found in previous reports (28, 29). In some experiments, the devices were interfaced with a Peltier heater (Mouser Electronic, CP50441) operated at 37 °C during use.

Microrobot Fabrication. Microrobots were fabricated at the University of Toronto Center for Microfluidic Systems cleanroom facility [using methods similar to those described previously (48) for other applications] to generate 3D, releasable microstructures. Briefly, 2 mL OmniCoat (MicroChem) was spin-coated on 4-inch-diameter silicon wafers at 2,500 rpm for 30 s, followed by a soft bake at 200 °C on a hot plate for 1 min. Next, 5 mL SU-8–2050 (MicroChem) was spin-coated (at 1,500, 2,500, or 5,500 rpm to form 100-, 50-, or 30-μm-thick layers, respectively) for 30 s, followed by a soft bake on a hotplate at 65 °C for 3 min and 95 °C for 8 min. The substrates were then exposed to UV radiation (11 mJ/cm^2 for 15 s) through a photomask and then postbaked at 65 °C for 2 min and 95 °C on a hot plate for 7 min, and finally immersed in SU8 developer for 7 min (MicroChem) to form an array of rigidly tethered microrobot structures. The substrates were then hard baked at 200 °C on a hot plate for 5 min and then immersed in Remover PG (MicroChem) for 2 min to dissolve the release layer. After gentle rinsing, the substrate bearing a loosely tethered array of microrobots was ready for use. In each experiment, 20 μL of liquid medium (see below) was pipetted onto a substrate and then gently aspirated back and forth to generate a suspension of microrobots. An aliquot (10 μL) of this microrobot suspension was loaded into the chamber of an OET device, followed by loading a second aliquot (10 μL) of bead or cell suspension. The medium used to generate suspensions of microrobots and polystyrene beads (15-μm-diameter, Polysciences) was deionized (DI) water containing 0.05% (vol/vol) Tween 20 (P9416 Sigma-Aldrich) (conductivity: 5.0 mS/m). The medium used to generate suspensions of cells was an aqueous sucrose buffer (DI water, 9 wt % sucrose, 0.3 wt % D-Glucose, 1.25% vol/vol PBS) (conductivity: 22.1 mS/m).

Cell Culture, Staining, and Loading into OET Devices. Base media were DMEM/F12 media (Life Technologies) (ARPE-19 cells) or DMEM media (Life Technologies) (MCF-7, B-16, and U-87 cells). Completed media were supplemented with 10% (vol/vol) FBS (FBS, Gibco) and 1% (vol/vol) penicillin and streptomycin (Invitrogen). Cells were grown in a humidified incubator filled with 5% (vol/vol) CO_2/air at 37 °C. Before use, ARPE-19 and MCF-7 cells were stained by adding 10 μM of CellTracker red CMFDA or CellTracker green CMPTZ (ThermoFisher Scientific) solution, respectively (diluted in the appropriate base media), and incubated for 30 min at 37 °C. B-16 and U-87 cells lines express the fluorescent proteins tdTomato (red) and eGFP (green), respectively (and thus were not stained). Before experiments, cells were washed twice in PBS (Life Technologies), passaged in 0.25% Trypsin-EDTA (Life Technologies), and finally centrifuged and resuspended in a sucrose buffer media at 0.1–1 × 10^6 cells per milliliter. Each suspension was filtered with a 40-μm cell strainer (Falcon), and different combinations of cells were mixed before loading into OET devices for experiments. Cells derived from mouse brain dissections were prepared and used as described in *SI Appendix*, in accordance with the *Guide to the Care and Use of Experimental Animals* (49) and approval of the Animal Care Committee at the University of Toronto (AUP 20011556).

ACKNOWLEDGMENTS. This research is supported by the Natural Sciences and Engineering Research Council of Canada (Grants RGPIN 2014-06042 and CREATE 482073-16), and the Local Innovative and Research Teams Project of Guangdong Pearl River Talents Program (Grant 2017BT01X121). The research is also supported by the University of Toronto's Medicine by Design initiative, which receives funding from the Canada First Research Excellence Fund. The authors acknowledge fruitful discussions with Dr. Steven Neale at University of Glasgow (UK), and thank Dr. Warren Chan at University of Toronto for access to transfected cell lines. A.R.W. and P.W.Z. acknowledge the Canada Research Chair (CRC) program.

1. Y. Chen *et al.*, A biologically inspired, flapping-wing, hybrid aerial-aquatic microrobot. *Sci. Robot.* **2**, eaao5619 (2017).
2. X. Yan *et al.*, Multifunctional biohybrid magnetite microrobots for imaging-guided therapy. *Sci. Robot.* **2**, eaaq1155 (2017).
3. J. Li, B. E.-F. de Ávila, W. Gao, L. Zhang, J. Wang, Micro/nanorobots for biomedicine: Delivery, surgery, sensing, and detoxification. *Sci. Robot.* **2**, eaam6431 (2017).
4. T. Wu *et al.*, A photon-driven micromotor can direct nerve fibre growth. *Nat. Photonics* **6**, 62–67 (2017).
5. M. J. Villangca, D. Palima, A. R. Bañas, J. Glückstad, Light-driven micro-tool equipped with a syringe function. *Light Sci. Appl.* **5**, e16148 (2016).
6. U. G. Būtaitė *et al.*, Indirect optical trapping using light driven micro-rotors for reconfigurable hydrodynamic manipulation. *Nat. Commun.* **10**, 1215 (2019).
7. S. Tottori *et al.*, Magnetic helical micromachines: Fabrication, controlled swimming, and cargo transport. *Adv. Mater.* **24**, 811–816 (2012).
8. J. Li *et al.*, Biomimetic platelet-camouflaged nanorobots for binding and isolation of biological threats. *Adv. Mater.* **30**, 1704800 (2018).
9. X. Wang *et al.*, MOFBOTS: Metal-Organic-Framework-Based biomedical microrobots. *Adv. Mater.* **6**, e1901592 (2019).
10. B. E.-F. de Ávila *et al.*, Hybrid biomembrane–functionalized nanorobots for concurrent removal of pathogenic bacteria and toxins. *Sci. Robot.* **3**, eaat0485 (2018).
11. M. Kaynak *et al.*, Acoustic actuation of bioinspired microswimmers. *Lab Chip* **17**, 395–400 (2017).
12. W. Wang *et al.*, Acoustic propulsion of nanorod motors inside living cells. *Angew. Chem. Int. Ed. Engl.* **53**, 3201–3204 (2014).
13. S. Mohanty, Optically-actuated translational and rotational motion at the microscale for microfluidic manipulation and characterization. *Lab Chip* **12**, 3624–3636 (2012).
14. J. Leach, H. Mushfique, R. di Leonardo, M. Padgett, J. Cooper, An optically driven pump for microfluidics. *Lab Chip* **6**, 735–739 (2006).
15. S. Maruo, H. Inoue, Optically driven micropump produced by three-dimensional two-photon microfabrication. *Appl. Phys. Lett.* **89**, 144101 (2006).
16. D. B. Phillips *et al.*, An optically actuated surface scanning probe. *Opt. Express* **20**, 29679–29693 (2012).
17. D. B. Phillips *et al.*, Shape-induced force fields in optical trapping. *Nat. Photonics* **8**, 400–405 (2014).
18. P. Y. Chiou, A. T. Ohta, M. C. Wu, Massively parallel manipulation of single cells and microparticles using optical images. *Nature* **436**, 370–372 (2005).
19. A. Jamshidi *et al.*, Dynamic manipulation and separation of individual semiconducting and metallic nanowires. *Nat. Photonics* **2**, 86–89 (2008).
20. M. C. Wu, Optoelectronic tweezers. *Nat. Photonics* **5**, 322–324 (2011).
21. R. Pethig, Review article-dielectrophoresis: Status of the theory, technology, and applications. *Biomicrofluidics* **4**, 022811 (2010).
22. M. Woerdemann, C. Alpmann, M. Esseling, C. Denz, Advanced optical trapping by complex beam shaping. *Laser Photonics Rev.* **7**, 839–854 (2013).
23. S. L. Neale, M. Mazilu, J. I. B. Wilson, K. Dholakia, T. F. Krauss, The resolution of optical traps created by light induced dielectrophoresis (LIDEP). *Opt. Express* **15**, 12619–12626 (2007).
24. S. Zhang, J. Juvert, J. M. Cooper, S. L. Neale, Manipulating and assembling metallic beads with optoelectronic tweezers. *Sci. Rep.* **6**, 32840 (2016).
25. J. K. Valley, A. Jamshidi, A. T. Ohta, H. Y. Hsu, M. C. Wu, Operational regimes and physics present in optoelectronic tweezers. *J. Microelectromech. Syst.* **17**, 342–350 (2008).
26. S. L. Neale *et al.*, Trap profiles of projector based optoelectronic tweezers (OET) with HeLa cells. *Opt. Express* **17**, 5232–5239 (2009).
27. S. Zhang *et al.*, Use of optoelectronic tweezers in manufacturing–Accurate solder bead positioning. *Appl. Phys. Lett.* **109**, 221110 (2016).
28. S. Zhang *et al.*, Patterned optoelectronic tweezers: A new scheme for selecting, moving, and storing dielectric particles and cells. *Small* **14**, e1803342 (2018).
29. S. Zhang *et al.*, Escape from an optoelectronic tweezer trap: Experimental results and simulations. *Opt. Express* **26**, 5300–5309 (2018).
30. A. R. Wheeler *et al.*, Microfluidic device for single-cell analysis. *Anal. Chem.* **75**, 3581–3586 (2003).
31. D. Di Carlo, L. Y. Wu, L. P. Lee, Dynamic single cell culture array. *Lab Chip* **6**, 1445–1449 (2006).
32. B. Dura *et al.*, Profiling lymphocyte interactions at the single-cell level by microfluidic cell pairing. *Nat. Commun.* **6**, 5940 (2015).
33. M. Poudineh *et al.*, Tracking the dynamics of circulating tumour cell phenotypes using nanoparticle-mediated magnetic ranking. *Nat. Nanotechnol.* **12**, 274–281 (2017).
34. H. Hwang, J. K. Park, Optoelectrofluidic platforms for chemistry and biology. *Lab Chip* **11**, 33–47 (2011).
35. L. Y. Ke *et al.*, Cancer immunotherapy μ-environment LabChip: Taking advantage of optoelectronic tweezers. *Lab Chip* **18**, 106–114 (2017).
36. J. K. Valley *et al.*, Optoelectronic tweezers as a tool for parallel single-cell manipulation and stimulation. *IEEE Trans. Biomed. Circuits Syst.* **3**, 424–431 (2009).
37. Y. H. Lin, G. B. Lee, An optically induced cell lysis device using dielectrophoresis. *Appl. Phys. Lett.* **94**, 033901 (2009).
38. C. Witte *et al.*, Spatially selecting a single cell for lysis using light-induced electric fields. *Small* **10**, 3026–3031 (2014).
39. P. A. Longo, J. M. Kavran, M. S. Kim, D. J. Leahy, Single cell cloning of a stable mammalian cell line. *Methods Enzymol.* **536**, 165–172 (2014).
40. L. Vermeulen *et al.*, Single-cell cloning of colon cancer stem cells reveals a multilineage differentiation capacity. *Proc. Natl. Acad. Sci. U.S.A.* **105**, 13427–13432 (2008).
41. S. Carroll, M. Al-Rubeai, The selection of high-producing cell lines using flow cytometry and cell sorting. *Expert Opin. Biol. Ther.* **4**, 1821–1829 (2004).
42. A. Gross *et al.*, Technologies for single-cell isolation. *Int. J. Mol. Sci.* **16**, 16897–16919 (2015).
43. C. Brasko *et al.*, Intelligent image-based in situ single-cell isolation. *Nat. Commun.* **9**, 226 (2018).
44. N. Nitta *et al.*, Intelligent image-activated cell sorting. *Cell* **175**, 266–276.e13 (2018).
45. G. Köhler, C. Milstein, Continuous cultures of fused cells secreting antibody of predefined specificity. *Nature* **256**, 495–497 (1975).
46. C. A. Cowan, J. Atienza, D. A. Melton, K. Eggan, Nuclear reprogramming of somatic cells after fusion with human embryonic stem cells. *Science* **309**, 1369–1373 (2005).
47. B. L. Coles-Takabe *et al.*, Don't look: Growing clonal versus nonclonal neural stem cell colonies. *Stem Cells* **26**, 2938–2944 (2008).
48. S. L. Neale, M. P. MacDonald, K. Dholakia, T. F. Krauss, All-optical control of microfluidic components using form birefringence. *Nat. Mater.* **4**, 530–533 (2005).
49. E. D. Olfert, B. M. Cross, A. A. McWilliam, Eds., *Guide to the Care and Use of Experimental Animals* (Canadian Council on Animal Care, 1993).